The mid-infrared luminosity function of galaxies in the European Large Area Infrared Space Observatory Survey southern fields

Article (Published Version)

The Astrophysical Journal, 609:122–132, 2004 July 1

THE MID-INFRARED LUMINOSITY FUNCTION OF GALAXIES IN THE EUROPEAN LARGE AREA *INFRARED SPACE OBSERVATORY* SURVEY SOUTHERN FIELDS

F. Pozzi,[1,2] C. Gruppioni,[2] S. Oliver,[3] I. Matute,[4,5] F. La Franca,[5] C. Lari,[6] G. Zamorani,[2] S. Serjeant,[7] A. Franceschini,[8] and M. Rowan-Robinson[9]

Received 2003 November 14; accepted 2004 March 11

ABSTRACT

We present the first determination of the 15 μm luminosity function of galaxies from the European Large Area *ISO* Survey (ELAIS) southern fields. We have adopted a new criterion to separate the quiescent, nonevolving and the starburst, evolving populations based on the ratio of mid-infrared to optical luminosity. Strong evolution is suggested by our data for the starburst galaxy population, while normal spiral galaxies are consistent with no evolution. The starburst population must evolve both in luminosity and in density with rates of the order $L(z) \propto (1+z)^{3.5}$ and $\rho(z) \propto (1+z)^{3.8}$, respectively, up to $z \sim 1$. The evolutionary parameters of our model have been tested by comparing the model predictions with other observables, like source counts at all flux density levels (from 0.1 to 300 mJy) and redshift distributions and luminosity functions at high z ($0.7 < z < 1.0$ from Hubble Deep Field North [HDF-N] data). The agreement between our model predictions and the observed data is remarkably good. We use our data to estimate the star formation density of the universe up to $z = 0.4$, and we use the luminosity function model to predict the trend of the star formation history up to $z = 1$.

Subject headings: galaxies: evolution — galaxies: luminosity function, mass function — galaxies: spiral — galaxies: starburst — infrared: galaxies

1. INTRODUCTION

The extragalactic background light shows that the emission from galaxies at infrared and submillimeter wavelengths is an energetically significant component of the universe. This emission originates from star formation activity and active galactic nuclei (AGNs). The precise contribution from each is still debated. It is thus important to our understanding of galaxy and AGN formation to study those populations that emit a substantial amount of light at infrared (IR) wavelengths in their rest frame. In particular, data from deep *Infrared Space Observatory* (*ISO*) surveys at 15 μm (i.e., Elbaz et al. 1999; Flores et al. 1999; Lari et al. 2001; Metcalfe et al. 2003) seem to require strong evolution for galaxies emitting in the infrared wavebands. This result, also supported by the detection of a substantial cosmic infrared background in the 140 μm–1 mm range (Puget et al. 1996; Hauser et al. 1998; Lagache et al. 1999), has stimulated the development of several evolutionary models for IR galaxies (i.e., Rowan-Robinson 2001; Franceschini et al. 2001; Chary & Elbaz 2001; Xu et al. 2003). All these models fit with different degrees of success the IR/submillimeter source counts and the cosmic infrared background within the present uncertainty limits but suffer from parameter degeneracy, and none of them is based on a local luminosity function (LLF) obtained from 15 μm data, since all were extrapolated from other IR wavelengths (12, 25, and 60 μm).

So far, complete spectroscopic samples of 15 μm sources have been obtained only in fields (i.e., HDF-N: Aussel et al. 1999; HDF-S: Mann et al. 2002, Franceschini et al. 2003) too small and too deep to allow a detailed study of the local luminosity function.

The European Large Area *ISO* Survey (ELAIS) is the largest open time project conducted by *ISO* (Oliver et al. 2000), mapping an area of $\approx$12 deg^2 at 15 and 90 μm. The final, band-merged ELAIS catalog has recently been completed (Rowan-Robinson et al. 2004). The spectroscopic data are most complete in the southern fields, and in this paper we present an analysis of the 15 μm luminosity function derived from these data. This is the first determination of the 15 μm luminosity function and its evolution, constrained by all the available observables in this band (source counts from *IRAS* to the deepest ISOCAM flux densities and redshift distributions at low and high z using data from both ELAIS and the deeper HDF-N survey). The model fitting the LF is then used to estimate the star formation history of the universe.

This paper is structured as follows. In § 2 we present our data sample. In § 3 we discuss the adopted IR and optical K-corrections. In § 4 we show the method used to compute the 15 μm LF and present the results. In § 5 we compare our LLF determination with previous ones. In § 6 we discuss the evolution rates derived from our data and compare the model predictions with the observable constraints and with other literature models. In § 7 we present our conclusions.

Throughout this paper we assume $H_0 = 75$ km s^{-1} Mpc^{-1}, $\Omega_m = 0.3$, and $\Omega_\Lambda = 0.7$, unless explicitly stated.

[1] Dipartimento di Astronomia, Università di Bologna, viale Berti Pichat 6, I–40127 Bologna, Italy.
[2] INAF–Osservatorio Astronomico di Bologna, via Ranzani 1, I–40127 Bologna, Italy.
[3] Astronomy Centre, Department of Physics and Astronomy, School of Science and Technology, University of Sussex, Brighton BN1 9QJ, UK.
[4] Max-Planck-Institut für extraterrestrische Physik, Postfach 1312, D-85741 Garching, Germany.
[5] Dipartimento di Fisica, Università "Roma Tre," via della Vasca Navale 84, I-00146 Rome, Italy.
[6] Istituto di Radioastronomia del CNR, via Gobetti 101, I-40129 Bologna, Italy.
[7] Centre for Astrophysics and Planetary Sciences, University of Kent, Canterbury, Kent CT 2 7NR, UK.
[8] Dipartimento di Astronomia, Università di Padova, vicolo dell'Osservatorio 2, I-35122 Padua, Italy.
[9] Astrophysics Group, Blackett Laboratory, Imperial College of Science, Technology and Medicine, Prince Consort Road, London SW7 2BW, UK.

2. THE DATA SAMPLES

2.1. *The Parent Catalogs*

Our analysis uses the southern ELAIS fields, which at present have more complete spectroscopy than the northern fields. S1 and S2 are the main survey fields in the southern hemisphere: S1 is centered at $\alpha(2000) = 00^{h}34^{m}44\overset{s}{.}4$, $\delta(2000) = -43^{\circ}28'12''$ and covers an area of $2^{\circ} \times 2^{\circ}$, while S2 is centered at $\alpha(2000) = 05^{h}02^{m}24\overset{s}{.}5$, $\delta(2000) = -30^{\circ}36'00''$ and covers an area of $21' \times 21'$.

The 15 μm data in these fields have been reduced using the LARI technique described in detail in Lari et al. (2001), and the 15 μm catalogs obtained in the two fields are given by Lari et al. and Pozzi et al. (2003), respectively. The source counts derived from the main field S1 are presented and discussed in Gruppioni et al. (2002). The whole S1 and S2 areas have been surveyed in the radio down to $S_{1.4\ \mathrm{GHz}} \approx 0.2$ and 0.13 mJy, respectively. The radio data analysis is presented in Gruppioni et al. (1999b) and P. Ciliegi et al. (2004, in preparation).

S1 contains 462 sources detected at 15 μm, 406 of which constitute a highly reliable sample that can be used in a conservative statistical analysis (see La Franca et al. 2004), while S2 contains 43 15 μm sources. Optical photometric follow-up has been obtained in S1 with the ESO/Danish 1.5 m telescope (to $R \sim 23$) and in S2 with the ESO Wide Field Imager (WFI) 2.2 m telescope in U, B, and I (to $I \sim 22$) and SOFI at the New Technology Telescope (NTT) in K' (to $K' \sim 18.75$). The spectroscopic follow-up was carried out at the Anglo-Australian Telescope (AAT) with Two-Degree Field (2dF) and ESO 3.6 m, NTT and Danish 1.5 m telescopes. In S1, $\sim$81% (328/406) of the 15 μm sources have an optical counterpart in the R band (taking into account all the optically identified sources to $R \sim 23$ plus six sources with $23 < R < 24.3$, see La Franca et al. 2004), while in S2, where the identification has been done in the I band, the percentage is higher ($\sim$90%, 39/43). In S1, the spectroscopic redshift completeness is $\sim$88% of identified objects and $\sim$71% of the whole sample (290 objects), while in S2 the corresponding figures are $\sim$77% and $\sim$70% (30 objects), respectively.

2.2. *The Spectroscopic Sample*

To study the 15 μm luminosity function and its evolution, we restrict our analysis to 15 μm sources with optical counterparts in the ranges of magnitude with higher spectroscopic identification completeness. Recalling the definition given in La Franca et al. (2004) of the S1_rest region (the shallower area) and of the S1_5 region (the deeper part), we consider the following objects: in S1_rest all the sources down to $R \leq 20.5$ (97% complete, 216/223); in S1_5 the sources down to $R \leq 21.6$ (97% complete, 73/75); in S2 the sources down to $R \leq 22.6$ and with 15 μm fluxes $\geq$1 mJy (100% complete, 18/18). In S2, the magnitude limit of $I \simeq 22$ can be converted (for uniformity with S1) to a limit in R magnitude, by assuming a mean color $R-I \sim 0.6$ (found for our galaxies). This leads to an R limit of $\sim$22.6 (see Pozzi et al. 2003). The conservative 15 μm cut is adopted in S2 because in this field there are uncertainties in the 15 μm completeness function below this flux level.

The sample of galaxies with measured redshift, after excluding objects classified as AGNs (both type 1 and type 2) or stars on the basis of their spectra, consists of 161 galaxies: 101 in S1_rest, 48 in S1_5, and 12 in S2. Following La Franca et al. (2004) and Pozzi et al. (2003), AGNs have been separated from galaxies according to classical diagnostic diagrams, and information on the nature of galaxy objects has been provided following the classification scheme of Dressler et al. (1999). This scheme is based primarily on two lines, [O II] λ3727 in emission and Hδ in absorption, which are good indicators of (respectively) current and recent star formation. Our sample of 161 galaxies includes 40 e(a) (spectra of dust-enshrouded starburst galaxies), 13 e(b) (spectra with very strong emission lines), 72 e(c) (spectra typical of spirals), 32 k(e) (spectra with signs of at least one emission line), and 4 k (spectra of elliptical-like objects) galaxies. In Figure 1 we show the magnitude versus 15 μm flux distribution of the whole S1_rest+S1_5+S2 sample of galaxies (objects with spectroscopic identification are shown with filled symbols).

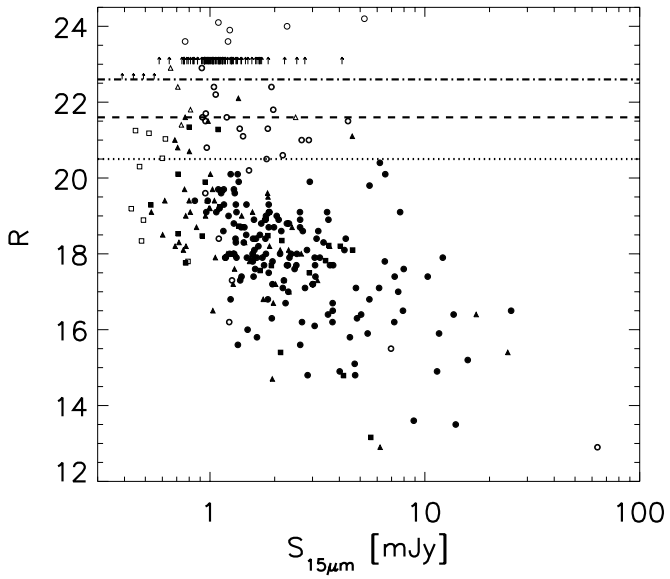

FIG. 1.—R-band magnitude as a function of 15 μm flux density for all 15 μm sources in the ELAIS southern fields. Sources with redshifts are shown as filled symbols, sources with likely optical counterparts but without redshifts are shown as open symbols, and sources without optical counterparts are shown as lower limits (*arrows*). Circles stand for sources from S1_rest, triangles for sources from S1_5, and squares for sources from S2. The three lines represent the three magnitude thresholds considered in this work (*dotted line*, S1_rest; *dashed line*, S1_5; *dot-dashed line*, S2).

In our estimates of the luminosity function and its evolution (§ 4), we apply an additional restriction, selecting only galaxies with redshift $z \leq 0.4$. As shown in Figure 4, above this redshift threshold the redshift distribution of galaxies is poorly sampled. The final total sample of galaxies considered for our LF determination consists of 150 objects.

3. THE *K*-CORRECTION

To derive the 15 μm luminosity function from our sample of galaxies, we need to relate the observed flux S (and redshift) to the rest-frame 15 μm and R-band luminosities. This requires knowledge of the K-correction in the mid-IR and in the R band.

Models of infrared-emitting populations (Rowan-Robinson 2001; Franceschini et al. 2001; Elbaz et al. 2002; Xu et al. 2003) have shown that the IR counts can be explained with three main populations. These populations are characterized by their spectral energy distributions (SEDs) and their evolutionary properties: normal spiral galaxies, starburst galaxies, and galaxies powered by an active galactic nucleus (AGNs). The three populations can be separated on the basis of their

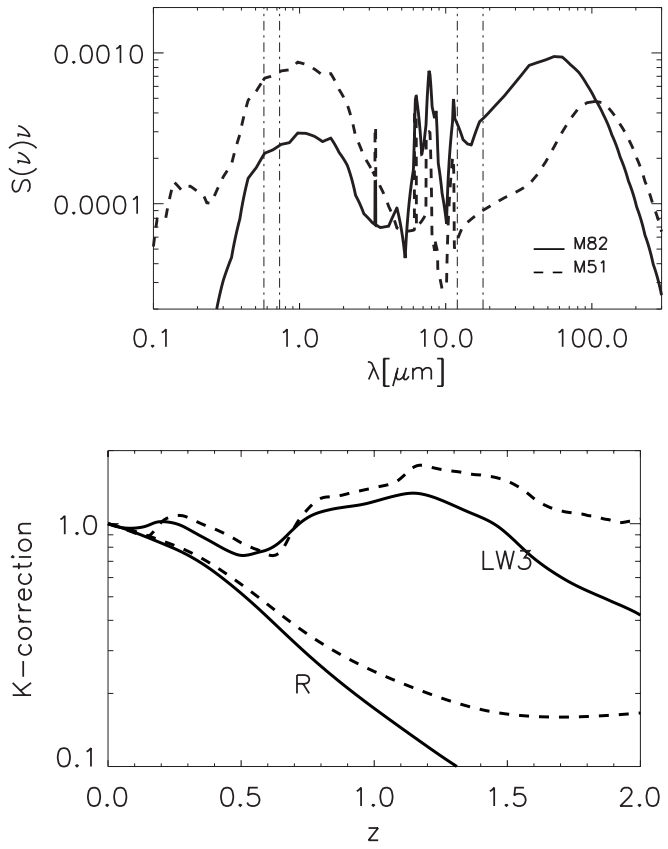

FIG. 2.—*Top*: Spectral energy distributions (SEDs) adopted for our galaxies. The dashed line corresponds to M51, a low-luminosity inactive spiral galaxy, while the solid line corresponds to M82, considered as the star-forming galaxy prototype. The SEDs have been taken from the GRASIL code (Silva et al. 1998). In the range from 5 to 18 μm, the SED for M82 is the observed ISOCAM CVF spectrum. The vertical dot-dashed lines correspond to the *R*-band and LW3 filter transmissions at the half-maximum–transmission values. *Bottom*: The *K*-correction as a function redshift in the LW3 and *R*-band filters for M51 (*dashed lines*) and M82 (*solid lines*).

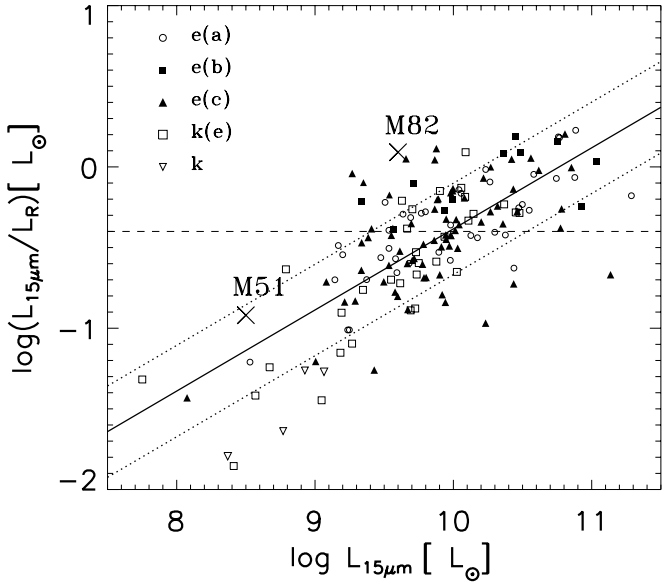

FIG. 3.—$L_{15\ \mu m}/L_R$ ratio as a function of $L_{15\ \mu m}$ for galaxies in the spectroscopic sample. Different symbols correspond to the different spectroscopic classes (see La Franca et al. 2004). The crosses represent the values for M51 and M82.

SEDs in the mid-IR/far-IR band (see Rowan-Robinson & Crawford 1989; Xu et al. 2003).

We have assumed M51 and M82 as prototypes of the normal and the starburst populations, respectively (the work on AGNs is presented in Matute et al. 2002; I. Matute et al. 2004, in preparation). M82 is a local moderate-starburst galaxy ($L_{IR} \sim 10^{10.6}\ L_\odot$; Elbaz et al. 2002). We did not consider the SEDs of a more active galaxy (like Arp 220, $L_{IR} \gtrsim 10^{11}\ L_\odot$), since from the identifications of ELAIS (La Franca et al. 2004) and HDF-N sources (Elbaz et al. 2002), such extreme galaxies are rare and tend to appear only at high redshift ($z \gtrsim 0.8$). The model SEDs of both M51 and M82 have been taken from the GRASIL model output (Silva et al. 1998) except for the mid-IR (5–18 μm) spectrum of M82, for which the observed ISOCAM Circular Variable Filter (CVF) spectrum (Förster Schreiber et al. 2003) has been adopted. The two reference SEDs (normalized to the bolometric luminosity from 0.1 to 1000 μm) and the corresponding *K*-corrections in the mid-IR filter (ISOCAM LW3 filter) and in the *R*-band filter (*R* Bessel) are shown in Figure 2. The normal spiral galaxy has relatively high far-IR over mid-IR emission and has a bolometric luminosity dominated by the optical region of the spectrum. The active galaxy has a bolometric luminosity dominated by the IR emission, as expected in presence of star formation obscured by larger amount of dust. As shown in Figure 2 (*bottom*), the two galaxies have similar *K*-corrections in the LW3 and *R*-band filters, at least up to $z \sim 1$.

Since in our sample we do not have the mid/far-IR colors, we have used the mid-IR to optical luminosity ratio to tentatively associate a representative SED (M51 or M82) to each galaxy. As discussed by La Franca et al. (2004), galaxies selected in the mid-IR band show a well-defined relation between the ratio of mid-infrared to optical luminosities ($L_{15\ \mu m}/L_R$) and the mid-infrared luminosities. This relation, although with some significant scatter, appears to hold over about 3 orders of magnitude in $L_{15\ \mu m}$, from the bright fluxes sampled by the IRAS sources (Rush et al. 1993) to the faintest ISO fluxes sampled in the HDF-S and HDF-N fields, with more infrared luminous galaxies having on average larger $L_{15\mu m}/L_R$ ratios. In first approximation, as suggested by the average SEDs shown in Figure 2, the ratio $L_{15\ \mu m}/L_R$ can be interpreted as an indication of the relative importance between bursting and more quiescent emission (see also Rowan-Robinson et al. 2004). In Figure 3 we plot the rest-frame $L_{15\ \mu m}/L_R$ versus $L_{15\ \mu m}$ for our galaxies (161 objects), where $L_{15\ \mu m}$ and L_R are the luminosities (νL_ν) at 15 μm and in the *R* band, respectively. The majority of our galaxies lie between the ratio values found for M51 and M82. On the basis of Figure 3, we have assumed $\log (L_{15\ \mu m}/L_R) \sim -0.4$ as the nominal separation between the normal and the starburst galaxy populations (*dot-dashed line*, see § 5 for a discussion). This leads to define subsamples of 81 spiral galaxies (80 at $z \leq 0.4$) and 80 (70 at $z \leq 0.4$) starburst galaxies. We did not use the spectroscopic classification to separate the two populations, since dust can significantly depress the emission features, which are mainly used to classify starburst galaxies, thus possibly leading to misleading classifications (see Rigopoulou et al. 2000; Franceschini et al. 2001). This is evident also from Figure 3 in which the different spectroscopic classes are not clearly segregated in different regions of the plot. In any case, it is reassuring that almost all the objects (12/13) spectroscopically classified as e(b) galaxies

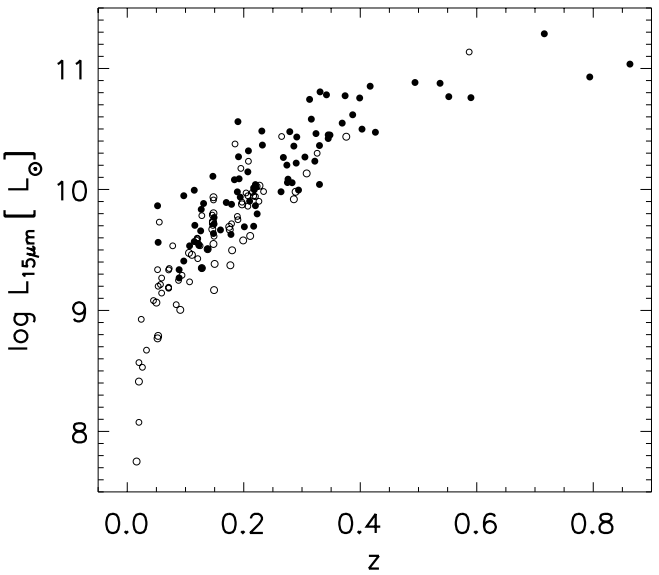

FIG. 4.—Rest-frame 15 μm luminosity as a function of redshift for galaxies in the spectroscopic sample. Open circles represent objects with $\log(L_{15\ \mu m}/L_R) < -0.4$ (defined as normal galaxies in this work); filled circles represent objects with $\log(L_{15\ \mu m}/L_R) > -0.4$ (defined as starburst galaxies in this work).

(spectra with very strong emission lines) do indeed have $\log(L_{15\ \mu m}/L_R) \gtrsim -0.4$ and all the objects (4/4) classified as k galaxies (elliptical-like spectra) have $\log(L_{15\ \mu m}/L_R) \lesssim -0.4$.

A least-square–fitting procedure applied to the data leads to the empirical relation

$$\log(L_{15\ \mu m}/L_R) = 0.50 \log L_{15\ \mu m} - 5.4, \quad (1)$$

with a dispersion of $\sim$0.28 dex. The best fit and its 1 σ bounds are shown in the figure as solid and dotted lines, respectively. This relation is discussed in detail in § 4.

In Figure 4 we show the $L_{15\ \mu m}$-z diagram. The normal and the starburst galaxies, as defined above, are represented by open and filled circles, respectively. The luminosity of each galaxy has been computed using the K-correction appropriate to its classification. Considering the galaxies up to $z = 0.4$, the median redshift of the whole sample (spiral plus starburst galaxies) is $z_{\rm med} \simeq 0.18$, while the median luminosity is $L_{15\ \mu m} \simeq 10^{9.8}\ L_\odot$. The majority of the normal galaxies lie at relatively low redshifts ($z_{\rm med} \simeq 0.14$) and luminosities ($L_{15\ \mu m} \simeq 10^{9.5}\ L_\odot$), while the active population is characterized by higher median values: $z_{\rm med} \simeq 0.23$, and $L_{15\ \mu m} \simeq 10^{10}\ L_\odot$.

4. THE MID-IR LUMINOSITY FUNCTION

4.1. *Estimator and Selection Effects*

The luminosity function and its evolution have been estimated using the parametric, unbinned, maximum likelihood method described in Marshall et al. (1983). We consider three different selection effects affecting our data: the 15 μm, the optical R-band, and the spectroscopic limits.

The 15 μm selection effect has been corrected for by weighting each data pair (z, $L_{15\ \mu m}$) by its 15 μm effective area [$\Omega(z, L_{15\ \mu m}) = \Omega(S)$]. The completeness functions for S1 and S1_5 are given in Table 1 of La Franca et al. (2004); for S2, we consider only fluxes greater than 1 mJy with an associated completeness of 93% for $1 < S < 2$ mJy and 100% for $S \geq 2$mJy (Pozzi et al. 2003).

The optical limits, reported in § 2.2, have been taken into account by introducing a function $\Theta(z, L_{15\ \mu m})$ which represents the probability that a source with a given 15 μm luminosity $L_{15\ \mu m}$ and redshift z had an R magnitude within the limits of the sample. To calculate the probability of any optical luminosity (L_R) given a specific data pair (z, $L_{15\ \mu m}$), we use the relation between the 15 μm and the optical luminosities together with its dispersion, assumed to be Gaussian (eq. [1]). The R-band K-correction described in § 3 has been used to relate the optical rest-frame luminosity to the observed magnitude.

The spectroscopic selection has been considered by weighting each triplet (z, $L_{15\ \mu m}$, L_R) by the spectroscopic completeness in the corresponding optical interval. This correction is not significant because of the high spectroscopic completeness in the considered optical intervals ($\gtrsim$95%, see § 2.2).

Following Marshall et al. (1983), the function to be minimized can be written as $S = -2 \ln \mathcal{L}$, where $\mathcal{L}$ is the likelihood function:

$$S = -2 \sum_{i=1}^{N} \ln \phi(z_i, L_i) + 2 \int\int \phi(z, L) \Omega(z, L) \Theta(z, L) \frac{dV}{dz}\, dz\, d \log L, \quad (2)$$

where L is the luminosity at 15 μm ($L_{15\ \mu m}$), N is the total number of sources in the three samples, $\Omega(z, l)$ is the available area of the sky for an object with luminosity L at redshift z, $\Theta(z, l)$ is the optical correction factor, (dV/dz) the differential volume element, and $\phi(z_i, L_i)$ is the luminosity function.

To optimally combine the information from the three different samples (S1_rest, S1_5, and S2), we follow the formalism described in Avni & Bahcall (1980). Each factor of the double integral of equation (2) is the sum of three terms:

$$\Omega(z, L)\Theta(z, L) = A_{S1} C_{S1}(z, L) \Theta_{S1}(z, L) + A_{S1\_5} C_{S1\_5}(z, L) \Theta_{S1\_5}(z, L) + A_{S2} C_{S2}(z, L) \Theta_{S2}(z, L) \quad (3)$$

where $A_{\rm S1}$, $A_{\rm S1\_5}$, and $A_{\rm S2}$ are the areas of the three fields (3.55, 0.55, and 0.12 deg^2 for S1, S1_5, and S2, respectively), $C_{\rm S1}$, $C_{\rm S1\_5}$, and $C_{\rm S2}$ are the three completeness functions, and $\Theta_{\rm S1}$, $\Theta_{\rm S1\_5}$, and $\Theta_{\rm S2}$ are the three optical factors.

Since we do not have enough data to assess different parametric forms, we decided to parameterize the luminosity function $\phi(l)$ using the form suggested by Saunders et al. (1990) as a good description of local 60 μm luminosity function of *IRAS* galaxies. By using a large sample of sources ($\sim$2800 objects), Saunders et al. (1990) found that a Schechter function was too narrow to describe IR-selected sources and a better fit could be achieved using the function

$$\phi(L) = \frac{dN(L, z = 0)}{dz\, d \log L} = \phi^* \left(\frac{L}{L_*}\right)^{1-\alpha} \exp\left\{-\frac{1}{2\sigma^2} \log_{10}^2 \left[1 + \left(\frac{L}{L_*}\right)\right]\right\} \quad (4)$$

In our likelihood analysis, we have searched for the best-fitting parameters of the local luminosity function and simultaneously tried to constrain the evolution of the mid-IR

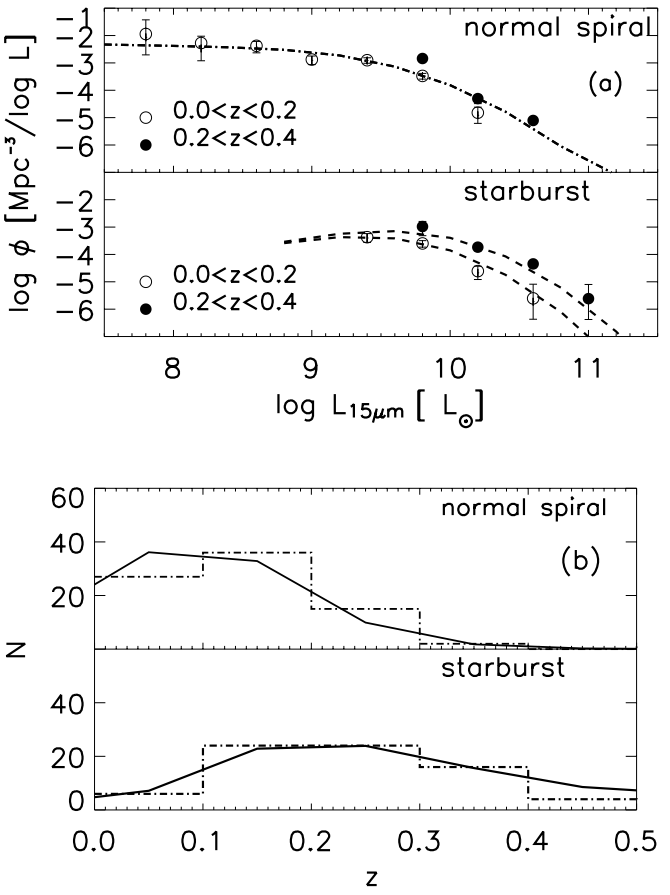

FIG. 5.—*Top*: Rest-frame 15 μm luminosity functions for the two galaxy classes from our survey in the two redshift bins $0.0 < z \leq 0.2$ and $0.2 < z \leq 0.4$. The open circles represent the $1/V_{\max}$ determination in the redshift interval 0.0–0.2, while the filled circles are in the interval 0.2 –0.4. *Upper plot*: normal galaxy population; *lower plot*: starburst population. *Bottom*: Comparison between the observed (*dot-dashed histogram*) and the predicted redshift distributions (*solid line*) for the two galaxy classes. *Upper plot*: normal galaxy population; *lower plot*: starburst population.

galaxies to reproduce the observed distribution of our data in the (z, $L_{15\ \mu\mathrm{m}}$) plane.

As suggested by Franceschini et al. (2001), the shape of the observed source counts (Euclidean from *IRAS* to a few mJy, followed by a sharp upturn at fainter fluxes) favors the hypothesis of strong evolution for only a fraction of the whole population, with the remaining galaxies giving rise to the Euclidean behavior. We have thus constrained our model by assuming that the spiral population does not evolve, while allowing the active galaxies (starbursts) to evolve both in density and in luminosity according to

$$\phi(L, z) = g(z)\phi(L/f(z), 0) \qquad (5)$$

parameterizing the two evolutions with two power laws: $g(z) = (1 + z)^{k_d}$ and $f(z) = (1 + z)^{k_l}$.

Since the likelihood method determines the shape and evolution of the luminosity function but not the overall normalization, we have normalized the two luminosity functions (for normal spiral and active galaxies) by requiring agreement between the predicted and the observed total number of sources for each class of objects.

4.2. *Results*

Figures 5*a* and 5*b* show the results of our ML best fit to the luminosity function of spiral and starburst populations in two different redshift bins: $0.0 < z \leq 0.2$ ($z_{\mathrm{mean}} \sim 0.12$) and $0.2 < z \leq 0.4$ ($z_{\mathrm{mean}} \sim 0.27$). The plotted data points correspond to the space densities of the observed sources computed independently with the $1/V_{\max}$ formalism (Schmidt 1968; Felten 1976).

The best-fitting parameters for the local luminosity functions of the two populations are reported in Table 1. The quoted errors correspond to the 1 σ confidence limit for each parameter calculated while allowing all the other parameters to vary ($\Delta\mathcal{L} = 1$, see Lampton et al. 1976). While for the starburst population we have allowed the evolution parameters to vary, as said before, we have assumed no evolution for the spiral component. For this reason, no error is reported for its evolution parameters. Support for this hypothesis is given by the $V/V_{\max}$ test (Schmidt 1968): in fact, under the hypothesis of no evolution we find $V/V_{\max} = 0.55 \pm 0.03$ for the normal spiral population and $V/V_{\max} = 0.64 \pm 0.03$ for the starburst population ($\gtrsim 4$ σ evidence of evolution). The latter value becomes 0.52 ± 0.03 assuming the evolution rates reported in Table 1.

Because of the relatively small number of objects in each population, the parameters derived from our maximum likelihood procedure are not very well constrained. This is true in particular for the evolutionary rates of the starburst population. In fact, although our data indicate strong evolution for this population, the uncertainties on the evolutionary parameters are largely because of the limited redshift interval covered by our surveys. For this reason, in order to better test the evolution, we have considered also other observables like source counts and redshift distributions at higher z, as discussed in § 6.

As shown in Figure 5*a*, the two populations sample different regions of the luminosity-redshift plane. In particular, the normal spiral population, which mainly comprises low-redshift and low-luminosity galaxies, samples well the faint end of the luminosity function, allowing an accurate determination of the α slope ($\sim$20% uncertainty, see Table 1). On the other hand, the starburst population samples well the high-luminosity, moderate–high-redshift regions. This allows the knee of the luminosity function to be better sampled and the L_* and σ parameters to be determined quite accurately. On the other hand, since we have not starburst galaxies at low luminosities (see Fig. 5), our data do not allow us to constrain, for this population, the α slope, which has been fixed to 0.0 as reported in Table 1.

TABLE 1

15 μm LUMINOSITY FUNCTION PARAMETERS FROM THE ML ANALYSIS

Population	α	σ	logL_*	logϕ^*	k_l	k_d
Normal spirals....	$1.10^{+0.25}_{-0.25}$	$0.5^{+0.1}_{-0.2}$	$8.8^{+0.7}_{-0.9}$	-2.45	0.0	0.0
Starbursts.....	0.0 (fixed)	$0.39^{+0.025}_{-0.025}$	$8.8^{+0.3}_{-0.2}$	-3.53	$3.5^{+1.0}_{-3.5}$	$3.8^{+2.0}_{-2.0}$

To test the consistency between our observed (z, $L_{15\ \mu m}$) distribution and that predicted from our parametric model, we have performed a two-dimensional Kolmogorov-Smirnov test (2D-KS, see Peacock 1983; Fasano & Franceschini 1987). The 2D-KS test gives $\geq$10% probability that the observed data are randomly sampled from the distributions predicted by the fitted LF.

4.3. *The Unidentified Objects*

In our maximum likelihood procedure, we have considered only objects with R brighter than our adopted limits and with $z \lesssim 0.4$ (150 objects). We have then corrected the remaining redshift incompleteness inside the considered magnitude range by applying weights to each galaxy with a spectroscopic redshift. In this way, we have assumed that the objects with no z (but within the R-magnitude limits) have the same properties (i.e., follow the same $L_{15\ \mu m}/L_R$ vs. $L_{15\ \mu m}$ relation) as the spectroscopically identified objects with similar R magnitude. Since the redshift completeness in the considered magnitude intervals is always very high ($\gtrsim$95%), we are confident that the uncertainties introduced are negligible.

A more delicate task is to deal with the 15 μm sources that have an R magnitude fainter than the selection limits or are unidentified (125 objects, $\sim$36% of the nonstellar sample; see La Franca et al. 2004 and Fig. 1). These sources could be either higher redshift sources or optically less luminous galaxies at redshift similar to those of the spectroscopically identified sample. In the first case, they are expected to follow the $L_{15\ \mu m}/L_R - L_{15\ \mu m}$ relation like the other galaxies, while this would not be the case for the second hypothesis.

Following La Franca et al. (2004), the first scenario seems more probable. The considerations discussed in La Franca et al. for this choice were mainly two: first, the $L_{15\ \mu m}/L_R$ versus $L_{15\ \mu m}$ seems to be a valid relation for all the mid-IR surveys from the ISOCAM ultradeep to the local *IRAS* surveys; and second, by estimating the redshift of the unidentified objects on the basis of the observed $\log z - R$ relation, the computed $L_{15\ \mu m}$ and L_R appear consistent with the assumed relation. In Figure 6, the observed redshift distribution of the spectroscopically identified objects and the estimated distribution (on the basis of the $\log z - R$ relation) of the unidentified sources is compared with the distribution predicted by our model (by extrapolating the results to high z, see § 6). In Figure 6, the agreement between the model predictions and the observed data (including the estimated distribution) is quite impressive. In particular, the estimated z-distribution of the unidentified sources is expected to fill exactly the secondary peak predicted by the model.

A further evidence supporting the hypothesis that most of the unidentified sources should belong to the same population as the identified sources, but with higher redshift ($z = 0.5-1.5$), is supplied by the photometric redshift technique. The photometric redshifts have been estimated and presented in the final band-merged ELAIS Catalog (Rowan-Robinson et al. 2004). The final band-merged catalog contains 1636 15 μm sources, 136 of which have $R \gtrsim 20.5$ (optical limit of our larger sample, S1_rest, see § 2.2) and enough optical data to determine photometric redshifts. The resulting photometric redshift distribution for all the ELAIS fields is in agreement with our hypothesis, showing that most of the 15 μm sources with associated faint optical galaxies are at significantly higher redshift than sources with brighter optical counterparts ($z_{\rm mean} = 0.75$ instead of $z_{\rm mean} = 0.2$ of the present optical bright sample).

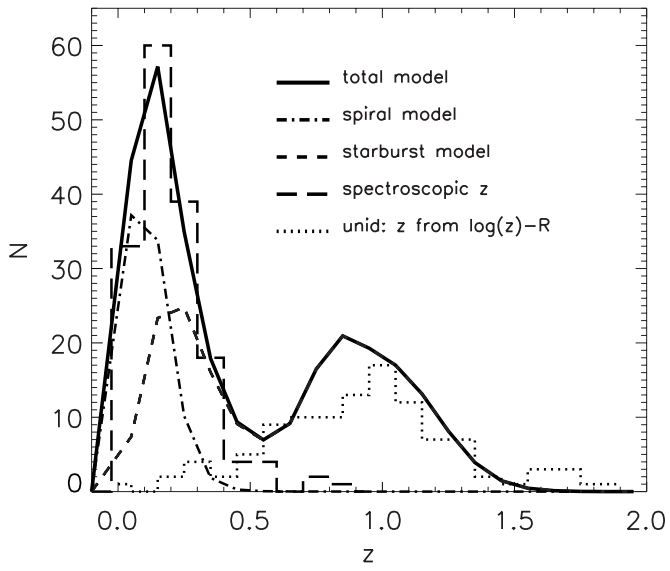

FIG. 6.—Comparison between the observed redshift distribution for the spectroscopically identified objects in the total S1_rest+S1_5+S2 sample (*long-dashed histogram*) and the model predictions (*solid line*). The contributions of the normal spiral and starburst components are shown as dot-dashed and dashed lines, respectively. The estimated distribution of the unidentified objects as given in La Franca et al. (2004) is also shown as a dotted line.

The bimodal behavior of the z distribution of the 15 μm sources shown in Figure 6 is caused by a combination of different causes: the shape of the LW3 K-correction (see Fig. 2), the high evolution rates found for the starburst population, and finally, the slope of the LF for high 15 μm luminosities. The dip in the redshift distribution around $z \approx 0.5$ is probably the cause of the gap around $R \sim 21$ in the distribution of the optical counterparts of the 15 μm sources (see Fig. 1 and the discussion in La Franca et al. 2004).

5. THE LOCAL LUMINOSITY FUNCTION

In Figure 7 the local luminosity function (LLF) of 15 μm galaxies (excluding AGNs) estimated in this work is compared with other determinations derived at different mid-IR bands and converted to 15 μm using our SEDs (M51 or M82, depending on galaxy type). Our estimate of the LLF has been done by extrapolating the result of the maximum likelihood method to $z = 0$ (*solid line*). To check the overall normalization, we have used the $1/V_{\rm max}$ formalism, "de-evolving" each galaxy according to the derived evolution coefficients (*filled circles*). In Table 2 the $1/V_{\rm max}$ LLF is listed, with $L_{15\ \mu m}$ defined as νL_ν and bin width $\delta \log (L_{15\ \mu m}) = 0.4$. The results of the two methods are consistent with each other, and the final $V/V_{\rm max}$ value for the total sample is $V/V_{\rm max} = 0.53 \pm 0.02$.

The open triangles are an estimate of the LLF of all galaxies (excluding Seyfert 1 and Seyfert 2) based on the 12 μm catalog of Rush et al. (1993). We have computed this LLF using the $1/V_{\rm max}$ method, selecting all galaxies with $S_{12\ \mu m} > 300$ mJy for which the 12 μm, optical, and spectroscopic completeness are 100% (see Rush et al. 1993). The dashed line is the LLF assumed by Franceschini et al. (2001), which is based on the 12 μm LLF computed by Fang et al. (1998) and re-adapted by Xu et al. (1998) in the low-luminosity regime. Franceschini et al. (2001) assume that starburst galaxies contribute $\sim$10% of the 12 μm LLF at all luminosities. Therefore we have converted their 12 μm LLF to 15 μm by using the

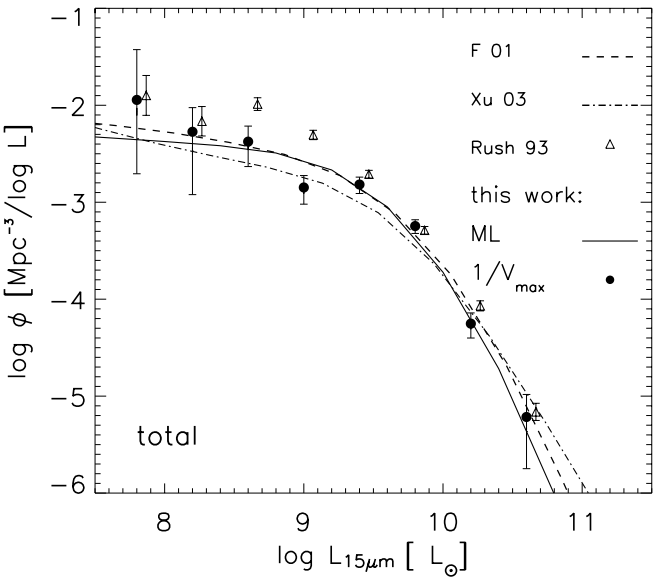

FIG. 7.—Local 15 μm luminosity function of galaxies. The filled circles are the $1/V_{\max}$ estimates from this work, while the solid line is the extrapolation to $z = 0$ of the ML results. The dashed line is the 12 μm LLF from Franceschini et al. (2001) (the Seyfert 2 contribution has been subtracted using the LLF for Seyfert 2 computed by Rush et al. 1993). The dot-dashed line is the 15 μm conversion of the LLF computed by Xu et al. (2003) at 25 μm. Open triangles are an estimate at 12 μm of the LLF of galaxies, based on the Rush et al. (1993) catalog. The LLF computed at mid-IR bands different from 15 μm have been converted to 15 μm as explained in the text.

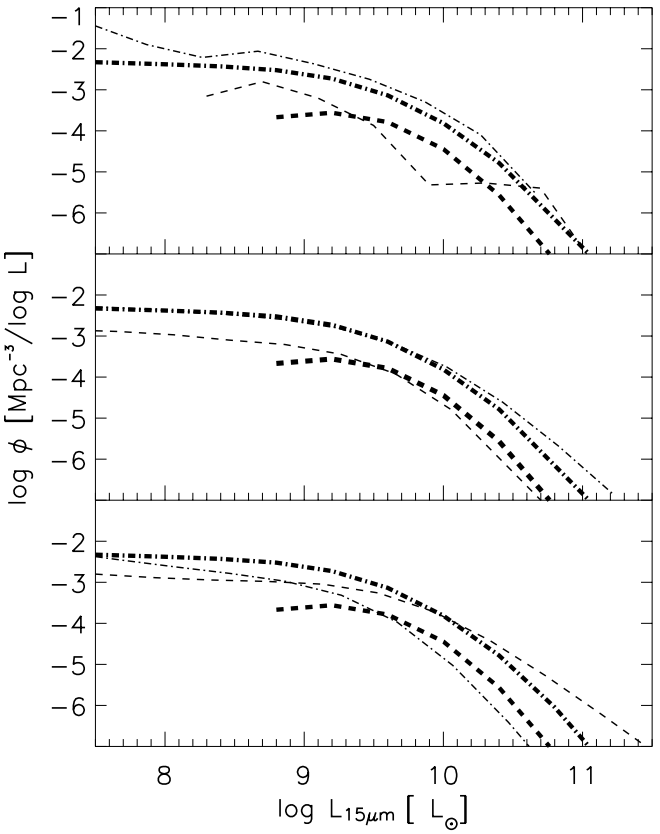

FIG. 8.—Comparison between the LLF subdivision into starburst and normal galaxy populations from this work and other analyses. The starburst galaxies are shown as dashed lines and the spirals as dot-dashed lines. The determinations from this work are the thicker lines. *Top*: comparison with Rush et al. (1993); *middle*: comparison with Franceschini et al. (2001) (the LLF computed by Rush et al. 1993 for the Seyfert 2 galaxies has been subtracted from the active component); *bottom*: comparison with Xu et al. (2003).

M82 and M51 SEDs for ~10% and ~90% of the 12 μm LLF, respectively. Moreover, since in the Franceschini et al. (2001) model the active population includes also the Seyfert 2 galaxies, we have obtained only the starburst contribution by subtracting the LLF of Seyfert 2 computed by Rush et al. (1993). Finally, the dot-dashed line is the LLF computed by Xu et al. (2001), which is based on the 25 μm sample of Shupe et al. (1998). This LLF is the sum of an actively star-forming and a normal population, defined by the *IRAS* colors.

As shown in Figure 7, the three independent estimates are reasonably consistent with each other. The differences in the low-luminosity regime between the Rush et al. (1993) and the other determinations is possibly caused by the effect of local inhomogeneities (particularly the Virgo supercluster) in the *IRAS* survey, as suggested by many authors (Fang et al. 1998; Xu et al. 1998). At high luminosity, the tendency of the Xu et al. (2001) LLF to be higher than the others is probably due to contamination from Seyfert 2 objects, which show IR colors similar to those of starbursts. The agreement between the overall normalization of our determination (based on the ISO data) and the other estimates based on *IRAS* data must be emphasized. This is indicative of a great accuracy both in the *ISO* calibration achieved with the LARI method (see Lari et al. 2001) and in the completeness corrections applied to our data.

While the total determinations of the mid-IR LLF for galaxies agree very well, their subdivisions into different populations (starburst and normal galaxies) made by different authors do not show the same level of consistency. In Figure 8 our LLF for the two galaxy populations (*thick lines*) are compared to those derived by Rush et al. (1993), Franceschini et al. (2001), and Xu et al. (2003) (*top*, *middle*, and *bottom panels, respectively*). The starburst populations are shown as dashed lines and the spiral ones as dot-dashed lines. The Rush et al. (1993) 12 μm LLF for normal galaxies (shifted to 15 μm through the M51 SED) is almost identical to our determination for the same population. Instead, the LLF of their liner+starburst component (the latter defined as sources with high-FIR luminosity) is significantly different from that estimated for our starburst population (basically it is much flatter than ours at $L_{15\ \mu\mathrm{m}} \gtrsim 10^{10}\ L_{\odot}$ and has a much higher volume density for the highest luminosity objects, $L_{15\ \mu\mathrm{m}} \sim 10^{11}\ L_{\odot}$). The Franceschini et al. (2001) LLF for galaxies are very similar to ours, both for starburst and normal spirals (also in this case, the LLF of Seyfert 2 computed by Rush et al. [1993] has been subtracted from the active component of Franceschini et al. [2001]). The Xu et al. (2003) populations' subdivision, derived from *IRAS* colors of 25 μm selected sources, is totally different, almost opposite to ours. In fact, their starburst LLF is higher than the

TABLE 2

15 μm LOCAL LUMINOSITY FUNCTION FROM THE $1/V_{\max}$ ANALYSIS

$\log[\nu L_{\nu}/L_{\odot}]$	$\log[\phi(\mathrm{Mpc}^{-3}\ \mathrm{mag}^{-1})]$	1 σ Error
7.8	−1.94	$^{+0.52}_{-0.76}$
8.2	−2.27	$^{+0.24}_{-0.64}$
8.6	−2.37	$^{+0.16}_{-0.25}$
9.0	−2.84	$^{+0.12}_{-0.17}$
9.4	−2.81	$^{+0.08}_{-0.09}$
9.8	−3.24	$^{+0.06}_{-0.08}$
10.2	−4.25	$^{+0.11}_{-0.14}$
10.6	−5.21	$^{+0.23}_{-0.53}$

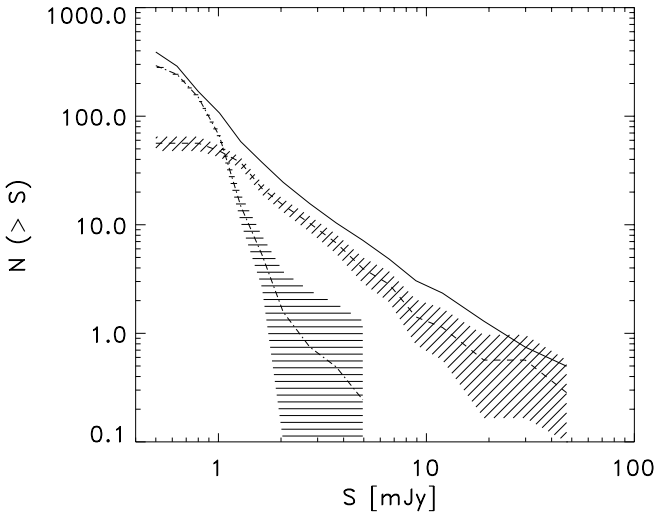

FIG. 9.—Contribution to the total integral source counts (*solid line*) from galaxies in the spectroscopic sample (*dashed line*) and from unidentified sources (*dot-dashed line*) in the ELAIS-S1 survey. The areas filled with horizontal and diagonal lines represent the 68% confidence regions. The confidence region for the total counts have not been shown for clarity.

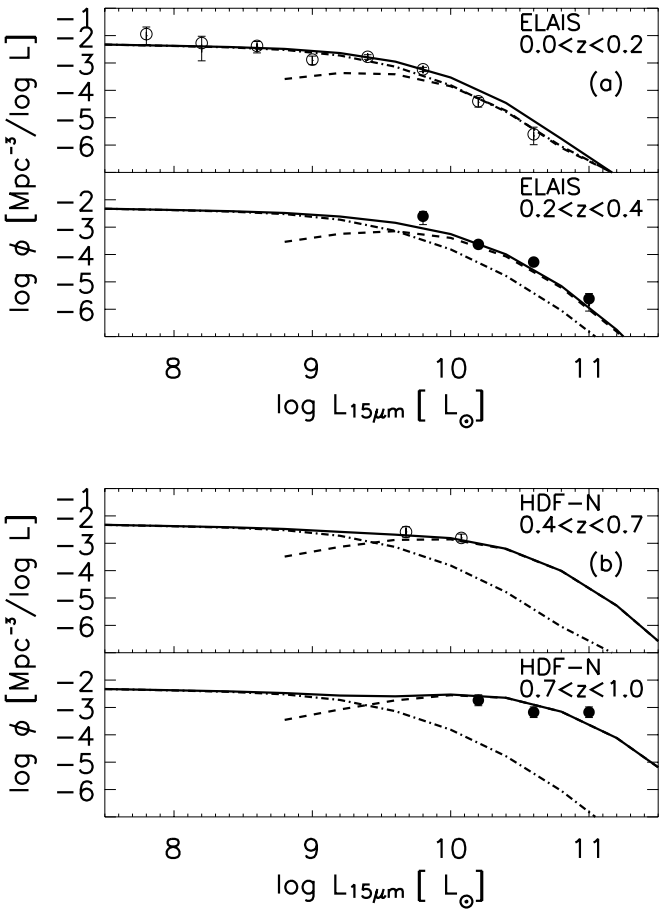

FIG. 10.—*Top*: Rest-frame 15 μm luminosity functions for the total sample of galaxies in the southern ELAIS fields (S1+S2). Dashed, dashed-dotted, and solid lines represent the starburst, normal galaxies, and total LFs from our model, respectively. *Upper plot*: $0.0 < z \leq 0.2$ ($z_{\rm mean} \simeq 0.12$); *lower plot*: $0.2 < z \leq 0.4$ ($z_{\rm mean} \simeq 0.27$). *Bottom*: The predicted rest-frame 15 μm luminosity functions extrapolated to higher redshift intervals and compared with data from the HDF-N survey. The points have been derived by C. Xu et al. (2003, private communication) from $1/V_{\rm max}$ analysis. *Upper plot*: $0.4 < z < 0.7$ ($z_{\rm mean} \simeq 0.55$); *lower plot*: $0.7 < z < 1.0$ ($z_{\rm mean} \simeq 0.85$).

normal galaxy one for $L > 10^9\ L_\odot$, and its high-luminosity slope is rather flat, producing a significant local contribution of starburst galaxies even at $L > 10^{10.5}$–$10^{11}\ L_\odot$. On the contrary, the Xu et al. (2003) normal galaxy LLF is lower and steeper at high luminosities than the starburst one and is more similar to our determination for starbursts. This significantly different subdivision, together with different evolutionary schemes proposed, is probably the main cause of the large difference in the model predictions between our work and that of Xu et al. (2003).

The populations' separation adopted in our work is based on a physical property of galaxies, like the ratio between mid-IR and optical luminosity. The choice of the value of the ratio ($R = L_{15\ \mu{\rm m}}/L_R$) chosen to divide the starburst from the normal spiral population is mainly based on two reasons. First, as previously said, it is between the value observed for M51 (normal spiral) and that observed for M82 (starburst galaxy). Second, it is the value that best allows to reproduce all the observables, from the normalization of the LLF to the redshift distributions at low and high z and source counts at all flux levels. A smaller fraction of the normal, nonevolving population ($\log R \lesssim -0.6$), while allowing better modeling of the sharp increase of the ELAIS-S1 counts (since a lower contribution of the spiral component would have been produced at mJy level), would have underestimated the total local luminosity function. On the contrary, a larger fraction of the normal population ($\log R \gtrsim -0.2$) would have enhanced the contribution of the quiescent component in the sources counts, predicting behavior too smooth with respect to the counts shape observed in the ELAIS-S1 field.

6. DISCUSSION ON EVOLUTION

As discussed in § 4.2, the redshift range sampled by the galaxies used to determine the LF of the two populations is too narrow ($0.0 < z \leq 0.4$) to constrain the evolution rates with a high degree of confidence. This is shown in Figure 9, in which the contribution of the galaxies used in the fitting procedure (*dashed line*) and of the unidentified objects (*dot-dashed line*) to the total observed source counts (*solid line*) are illustrated separately. The spectroscopic sample contributes only marginally to the large excess with respect to the Euclidean expectations at $\sim$1 mJy, which is indeed dominated by optically unidentified sources. For this reason, to test our evolution rates, we have compared the predictions of our model with other observables, extending the analysis to lower flux densities and higher z than those reached by our survey (using the source counts and the HDF-N data set). We have extrapolated the model results to higher redshift, given the evidence reported in § 4.3 that all the 15 μm sources belong to the same population of galaxies.

6.1. *Comparison between Model Predictions and Data*

We find that the agreement between the model predictions and the observables is very good. In particular, the starburst population must evolve with the evolution rates found ($k_l \sim 3.5$ and $k_d \sim 3.8$, see Table 1) up to $z_{\rm break} \sim 1$ and no additional evolution at $z > z_{\rm break}$. Of course, the k_l and k_d values depend on how the different galaxy populations emitting in the mid-IR band are separated. However, once the subdivision is fixed, the evolution rates are well determined, given the large number of observables to be fitted.

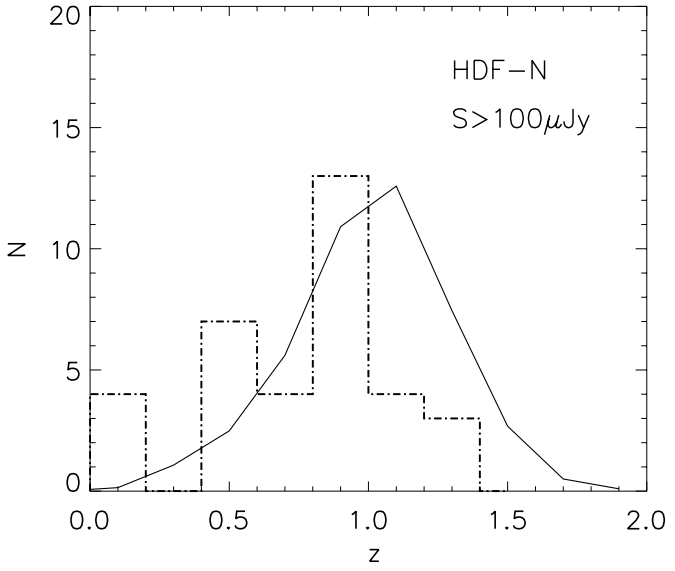

FIG. 11.—Comparison between the observed (*dot-dashed histogram*) and the predicted redshift distributions (*solid line*) in the HDF-N field. Sources with $S \geq 0.10$ mJy have been considered (41 objects; H. Aussel and S. Berta, 2003, private communication).

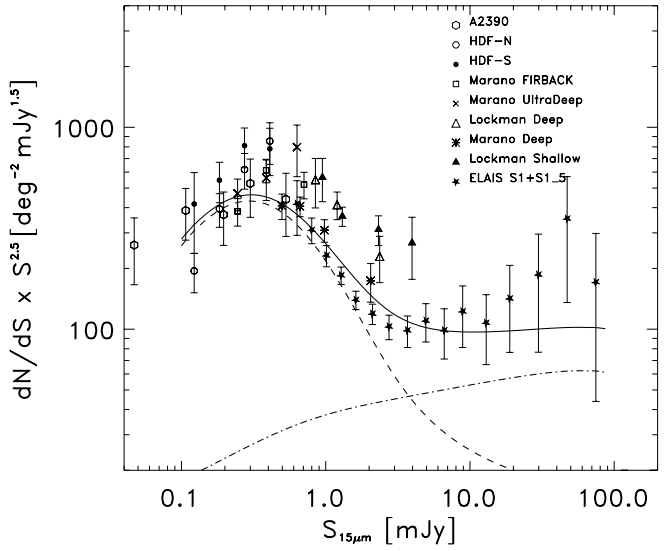

FIG. 12.—Comparison of model prediction and observed 15 μm source counts. Data points: *filled stars*, ELAIS-S1 counts reported by Gruppioni et al. (2002); *open diamonds*, new A2390 source counts from Metcalfe et al. (2003). Other data points from Elbaz et al. (1999): *open circles*, *ISO* HDF-N; *filled circles*, *ISO* HDF-S; *open squares*, Marano Firback; *crosses*, Marano Ultra-Deep; *asterisks*, Marano Deep; *open triangles*, Lockman Deep; *filled triangles*, Lockman Shallow. Dashed and dashed-dotted lines represent the contributions from starburst and normal galaxies, respectively, computed with our model.

In Figures 10*a* and 10*b*, the total (normal spiral+starburst) luminosity functions predicted by our model in the ELAIS southern fields (our sample) and in the HDF-N field are compared with the data. For the shallower ELAIS fields, the observed and predicted luminosity functions have been computed in two low-redshift bins: $0.0 < z \leq 0.2$ ($z_{\rm mean} \sim 0.12$) and $0.2 < z \leq 0.4$ ($z_{\rm mean} \sim 0.27$). For the deeper HDF-N, the observed and predicted luminosity functions are computed in two higher redshift bins: $0.4 < z < 0.7$ ($z_{\rm mean} \sim 0.55$) and $0.7 < z < 1.0$ ($z_{\rm mean} \sim 0.85$). In the latter redshift bins, the model is an extrapolation to higher redshift of our best-fitting model; the data points are from C. Xu et al. (2003, private communication) in which they were computed using the $V_{\rm max}$ formalism.

In Figure 11 the redshift distribution of sources with $S > 0.1$ mJy predicted by our model is superimposed on the data to the same flux density limit observed in the HDF-N. The agreement between the observed and the modeled distributions is very good, both in shape and normalization, with both distributions showing a peak around $z \sim 0.9-1.0$.

In Figure 12 the observed and the predicted differential source counts are compared. Our model reproduces well the trend observed from the *IRAS* flux densities down to the ultradeep survey limits and is in perfect agreement with our ELAIS data at fluxes $S_{15\ \mu{\rm m}} \lesssim 1$ mJy and $\gtrsim 3$ mJy, while it is slightly higher and smoother than our data in the critical interval $1 \lesssim S_{15\ \mu{\rm m}} \lesssim 3$ mJy, in which the counts start diverging from no-evolution expectations and data from different surveys show larger differences. Our model is, however, between, and consistent within the errors, with both ELAIS data and those reported by Elbaz et al. (1999) and Metcalfe et al. (2003). The sharp upturn shown by the ELAIS source counts around 2 mJy could be reproduced well by Gruppioni et al. (2002) by introducing a luminosity cutoff in the local luminosity function of starburst galaxies at $L = 10^{10.8}\ L_{\odot}$. Although our data cannot either confirm or rule out this hypothesis, in the present work we have chosen not to introduce any "artificial" constraint in our maximum likelihood luminosity function determination.

6.2. *Comparison with Other Evolutionary Models*

The idea of modeling the mid-IR source counts and luminosity function by dividing the sources into different populations following different evolutionary schemes was first proposed by Franceschini et al. (2001). The Franceschini et al. and our local population subdivisions are similar (see § 5), although the evolutionary rates required by Franceschini et al. for the starburst population are slightly higher than ours: $\sim(1+z)^{3.8}$ in luminosity and $\sim(1+z)^4$ in density. For this reason, the source counts predicted by Franceschini et al. are somewhat higher and smoother than ours, especially in the flux density interval $1 < S < 5$ mJy, and their modeled redshift distribution, although similar at faint flux densities (i.e., $S_{15\ \mu{\rm m}} \geq 0.1$ mJy in the HDF-N), shows a significant peak around $z \simeq 0.8-1$, even at relatively high flux densities ($\gtrsim 2$ mJy and up to 10 mJy), not observed in the data. Despite these differences, the Franceschini et al. model is the model, which among all those existing in the literature produces results more similar to ours.

For example, the recent model of Xu et al. (2003) predicts source counts that are not only significantly higher than our expectations but also higher than all the 15 μm source counts derived by the different mid-IR surveys over a large flux density interval ($1 \lesssim S_{15\ \mu{\rm m}} \lesssim 10$ mJy). The large discrepancy between Xu et al. (2003) and our models might be due to a combination of several causes, including a different population subdivision of the local luminosity function (see Fig. 8) and a different AGN contribution. As shown in § 5, the local luminosity function of starburst galaxies derived by Xu et al. (2003) (see Fig. 8) has a very pronounced high-luminosity tail in contrast with our determination. This tail causes the high predicted counts at a few mJy, since local galaxies, characterized by $L_{15\ \mu{\rm m}} \sim 10^{11}\ L_{\odot}$ and undergoing a moderate-high evolution, at a typical redshift of $z \sim 1$

would have $L_{15\ \mu m}(z \sim 1) \sim 8-10 L_{15\ \mu m}(z = 0)$ and flux densities in the mJy range. On the contrary, local starburst galaxies with typical luminosities of $L_{15\ \mu m} \lesssim 10^9-10^{10}\ L_\odot$ (as in our model) would have $L_{15\ \mu m} \sim 10^{11}\ L_\odot$ at $z \sim 1$ and expected fluxes in the sub-mJy range ($S \sim 0.4$ mJy), in which the bump observed in the differential counts is located. Moreover, the evolution considered by Xu et al. (2003) for AGN is higher than that found by I. Matute (2004, private communication).

Although all the models give rise to different results, it is interesting to note that they all agree in the determination of the total local luminosity function (see § 5), although with different population subdivisions and/or evolution hypotheses.

6.3. *Star Formation History Predicted by Model*

The evolving luminosity function model can be used to determine the star formation rate density of the universe. We first calculate the luminosity density at 15 μm by integrating the luminosity function over all the luminosities; then we convert the luminosity density into star formation density using the star formation calibrator based on mid-IR data. To this purpose, we have used the calibration given by Mann et al. (2002) for a Salpeter (1955) IMF, over the mass range [0.1,100] $M_\odot$. Since the Mann et al. (2002) infrared estimator is based on the $L_{60\ \mu m}$ bolometric luminosity [$\mathrm{SFR}(M_\odot\ \mathrm{yr}^{-1}) = \lambda L_\lambda(60\ \mu\mathrm{m})/1.5 \times 10^{36}$ W], $L_{15\ \mu m}$ has been converted to $L_{60\ \mu m}$ following Mazzei et al. (2001) ($L_{60\ \mu m}/L_{15\ \mu m} \sim 5$). The adopted value is consistent within ~20%–30% with the values of M51 and M82 (see Fig. 2). In the same way, we have also translated into star formation rate (SFR) density the $1/V_{\max}$ luminosity function results derived in two redshift bins ($0.0 < z \leq 0.2$ and $0.2 < z \leq 0.4$).

In Figure 13 we show a compilation of estimates on the star formation rate density as a function of redshift from different indicators taken from Somerville et al. (2001) in a $\Omega_m = 0.3$, $\Omega_\Lambda = 0.7$ cosmology in units of $h\ M_\odot\ \mathrm{yr}^{-1}\ \mathrm{Mpc}^{-3}$. The UV data have been corrected for dust extinction following Somerville et al. (2001), while the Hα data have been corrected for dust extinction by the original authors. The estimates derived from mid-IR data in the HDF-S by Mann et al. (2002) and from radio data by Haarsma et al. (2000) have also been added, after conversion to the adopted cosmology. The prediction of our model is shown as a solid line and the $1/V_{\max}$ data points as filled circles.

Our model predicts a trend for the star formation density similar to the results obtained in other bands, with a rapid increase from $z \sim 0$ to $z \sim 1$, followed by a flat plateau at high z. The actual measured data points at $z \leq 0.4$ are of particular interest, since they provide an estimate of the star formation density at a relatively low redshift but not so local to be affected by clustering and local inhomogeneities. We found star formation densities of $\dot{\rho} = 0.025 \pm 0.007$ and $0.043 \pm 0.020\ h\ M_\odot\ \mathrm{yr}^{-1}\ \mathrm{Mpc}^{-3}$ at the two average redshifts $z = 0.12$ and 0.27, respectively. At $0.4 \lesssim z \lesssim 1.0$, where the ELAIS data are highly incomplete, the model has been constrained by other high-z observables in literature. We do not extrapolate the predictions of our model to $z > 1.3$, since the LW3 ISO filter does not allow efficiently sampling of this redshift range (see LW3 K-correction in the Fig. 2). Our model prediction is consistent with the estimates derived from UV, optical, and mid-IR data up to $z \leq 0.4$. In particular, our results are in excellent agreement with the data result obtained by Mann et al. (2002) from the mid-IR survey in the HDF-S (Fig. 13, *filled downward-pointing triangles*). At $0.4 \lesssim z \lesssim 1.0$, the model is significantly higher than the extinction-corrected UV data, suggesting that the extinction corrections applied could be underestimated at those redshifts. The estimates derived from radio data by Haarsma et al. (2000) (*filled squares*) are systematically higher than our model predictions by about a factor of 2. However, these data might be overestimated, since the authors also considered as star-forming galaxies (thus contributing to the star formation density) all the unidentified radio sources, even at flux densities for which the fraction of elliptical radio galaxies could still be significant (see Gruppioni et al. 1999a).

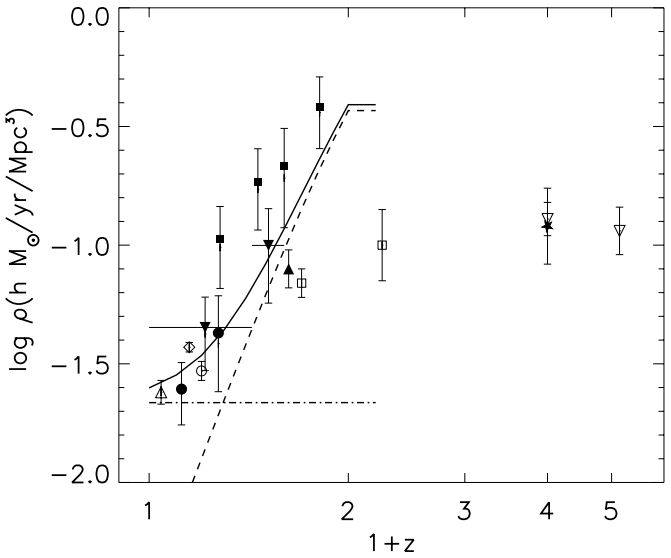

FIG. 13.—Compilation of constraints on the star formation history of the universe mainly taken from Somerville et al. (2001). The UV data have been corrected for dust extinction following Somerville et al. (2001), while the Hα data have been corrected by the original authors. In all cases a $\Omega_m = 0.3$, $\Omega_\Lambda = 0.7$ cosmology and a Salpeter (1955) IMF over the mass range [0.1, 100] $M_\odot$, were assumed. Units are $h\ M_\odot\ \mathrm{yr}^{-1}\ \mathrm{Mpc}^{-3}$. The filled circles and the solid curve are from this work ($1/V_{\max}$ analysis of ELAIS data and prediction of our maximum likelihood model, the dashed and the dot-dashed lines being the contribution of starbursts and spirals, respectively). The symbols are: *open upward-pointing triangles*, Gronwall (1998); *open circles*, Tresse & Maddox (1998); *open diamonds*, Treyer et al. (1998); *filled downward-pointing triangles*, Mann et al. (2002); *filled upward-pointing triangles*, Flores et al. (1999); *filled squares*, Haarsma et al. (2000); *open squares*, Cowie et al. (1996); *open downward-pointing triangles*, Steidel et al. (1999); *filled stars*, Hughes et al. (1998).

7. CONCLUSION

We have presented the first direct determination of the 15 μm luminosity function and its cosmic evolution for galaxies. As previously found by other authors, three populations of sources give rise to the 15 μm emission: the normal, the starburst, and the AGN populations, characterized by different cosmic evolution. In this work we have analyzed the galaxy component only (quiescent plus actively star-forming). The contribution of the AGN component is discussed in a separate paper (Matute et al. 2002; I. Matute et al. 2004, in preparation).

The analysis is based on data from the ELAIS southern fields survey. The sample is ~150 galaxies in the redshift interval $0.0 < z \leq 0.4$ and covers a large flux density range between the *IRAS* and the deep ISOCAM surveys ($0.5 \leq S \leq 50$ mJy). Unlike other authors, we have adopted in this work the $L_{15\ \mu m}/L_R$ ratio as a criterion to separate the quiescent,

nonevolving and the starburst, evolving populations. This criterion, suggested by the existing correlation between $L_{15\ \mu m}/L_R$ and the amount of activity in galaxies, is a posteriori supported by the results of the V/V_{max} analysis of the two populations defined on this basis.

The main results of our analysis are:

1. In the ML analysis we have simultaneously fitted both the evolution rates and the shape parameter of the local LF for both the spiral and the starburst populations. We have assumed that the spiral population does not evolve, while we have let evolve the starburst population both in luminosity and in density. Since the two populations sample different luminosity ranges, we have obtained an accurate determination for the faint end of the LLF for the quiescent component, while the knee and the σ parameters of the LLF are better constrained for the starbursts. The evolution found for the active population is $\sim(1+z)^{3.5}$ in luminosity and $\sim(1+z)^{3.8}$ in density, up to $z_{break} \sim 1$.

2. Our total 15 μm LLF is in agreement with previous determinations derived from the *IRAS* data. On the contrary, the LLFs for different populations derived by different authors do not have the same level of consistency. While in our subdivision the quiescent population is expected to dominate locally over all the luminosity range, in other models (i.e., Xu et al. 2003) the starburst population dominates locally at high luminosities, leading to a large discrepancy in the model predictions.

3. To test the evolution parameters with a higher degree of confidence, we have compared our model predictions with all the observables existing in literature over all the z and flux ranges (source counts, luminosity functions, and z distributions). Our best-fitting model reproduces well all the observables. In the critical interval $1 \lesssim S \lesssim 3$ mJy, in which the source counts from different surveys show larger discrepancies, our model is between the data from ELAIS-S1 (Gruppioni et al. 2002) and that from the deep surveys (Elbaz et al. 1999). On the other hand, in the flux range $3 \lesssim S \lesssim 10$ mJy, our model is consistent with existing data, unlike the Xu et al. (2003) model, whose predicted differential sources counts are at least a factor of 3 higher than the data.

4. Using the evolutionary model found for the 15 μm galaxies and the data points from the $1/V_{max}$ LF analysis, we have estimated the star formation rate density. The redshift range sampled by our data ($0.0 < z \leq 0.4$) is of particular interest, since it provides an estimate of the star formation at relatively low redshift but is not so local to be affected by clustering and local dishomogeneities. We find $\dot{\rho} = 0.025 \pm 0.007$ and $0.043 \pm 0.020\ h\ M_\odot\ \mathrm{yr}^{-1}\ \mathrm{Mpc}^{-3}$ at the two mean redshifts $z = 0.12$ and 0.27, respectively. At $z \lesssim 0.4$ our model predictions are consistent with other estimates derived from UV, optical, and mid-IR data. At higher redshift our model predictions are significantly higher than the UV extinction– corrected data and lower by about a factor of 2 than the estimates derived from radio data by Haarsma et al. (2000).

F. P. was partially supported by the European Program Human Potential (contract HPMT-CP-2000-00096). F. P. would like to thank Lucia Pozzetti for helpful discussion.

REFERENCES

Aussel, H., Elbaz, D., Cesarsky, C. J., & Starck, J. L. 1999, in The Universe as Seen by *ISO*, ed. P. Cox & M. F. Kessler (ESA SP-427; Noordwijk: ESA), 1023
Avni, Y., & Bahcall, J. N. 1980, ApJ, 235, 694
Chary, R., & Elbaz, D. 2001, ApJ, 556, 562
Cowie, L. L., Songaila, A., Hu, E. M., & Cohen, J. G. 1996, AJ, 112, 839
Dressler, A., Smail, I., Poggianti, B. M., Butcher, H., Couch, W. J., Ellis, R. S., & Oemler, A. J. 1999, ApJS, 122, 51
Elbaz, D., Cesarsky, C. J., Chanial, P., Aussel, H., Franceschini, A., Fadda, D., & Chary, R. R. 2002, A&A, 384, 848
Elbaz, D., et al. 1999, A&A, 351, L37
Fang, F., Shupe, D. L., Xu, C., & Hacking, P. B. 1998, ApJ, 500, 693
Fasano, G., & Franceschini, A. 1987, MNRAS, 225, 155
Felten, J. E. 1976, ApJ, 207, 700
Flores, H., et al. 1999, ApJ, 517, 148
Förster Schreiber, N. M., Sauvage, M., Charmandaris, V., Laurent, O., Gallais, P., Mirabel, I. F., & Vigroux, L. 2003, A&A, 399, 833
Franceschini, A., Aussel, H., Cesarsky, C. J., Elbaz, D., & Fadda, D. 2001, A&A, 378, 1
Franceschini, A., et al. 2003, A&A, 403, 501
Gronwall, C. 1998, in ASP Conf. Ser. 146, The Young Universe: Galaxy Formation and Evolution at Intermediate and High Redshift, ed. S. D'Odorico, A. Fontana, & E. Giallongo (San Franciscso: ASP), 96
Gruppioni, C., Lari, C., Pozzi, F., Zamorani, G., Franceschini, A., Oliver, S., Rowan-Robinson, M., & Serjeant, S. 2002, MNRAS, 335, 831
Gruppioni, C., Mignoli, M., & Zamorani, G. 1999a, MNRAS, 304, 199
Gruppioni, C., et al. 1999b, MNRAS, 305, 297
Haarsma, D. B., Partridge, R. B., Windhorst, R. A., & Richards, E. A. 2000, ApJ, 544, 641
Hauser, M. G., et al. 1998, ApJ, 508, 25
Hughes, D. H., et al. 1998, Nature, 394, 241
La Franca, F., et al. 2004, AJ, in press (astro-ph/0403211)
Lagache, G., Abergel, A., Boulanger, F., Désert, F. X., & Puget, J.-L. 1999, A&A, 344, 322
Lampton, M., Margon, B., & Bowyer, S. 1976, ApJ, 208, 177
Lari, C., et al. 2001, MNRAS, 325, 1173
Mann, R. G., et al. 2002, MNRAS, 332, 549
Marshall, H. L., Tananbaum, H., Avni, Y., & Zamorani, G. 1983, ApJ, 269, 35
Matute, I., et al. 2002, MNRAS, 332, L11
Mazzei, P., Aussel, H., Xu, C., Salvo, M., De Zotti, G., & Franceschini, A. 2001, NewA, 6, 265
Metcalfe, L., et al. 2003, A&A, 407, 791
Oliver, S., et al. 2000, MNRAS, 316, 749
Peacock, J. A. 1983, MNRAS, 202, 615
Pozzi, F., et al. 2003, MNRAS, 343, 1348
Puget, J.-L., Abergel, A., Bernard, J.-P., Boulanger, F., Burton, W. B., Desert, F.-X., & Hartmann, D. 1996, A&A, 308, L5
Rigopoulou, D., et al. 2000, ApJ, 537, L85
Rowan-Robinson, M. 2001, ApJ, 549, 745
Rowan-Robinson, M., & Crawford, J. 1989, MNRAS, 238, 523
Rowan-Robinson, M., et al. 2004, MNRAS, in press (astro-ph/0308283)
Rush, B., Malkan, M. A., & Spinoglio, L. 1993, ApJS, 89, 1
Salpeter, E. E. 1955, Vistas Astron., 1, 283
Saunders, W., Rowan-Robinson, M., Lawrence, A., Efstathiou, G., Kaiser, N., Ellis, R. S., & Frenk, C. S. 1990, MNRAS, 242, 318
Schmidt, M. 1968, ApJ, 151, 393
Shupe, D. L., Fang, F., Hacking, P. B., & Huchra, J. P. 1998, ApJ, 501, 597
Silva, L., Granato, G. L., Bressan, A., & Danese, L. 1998, ApJ, 509, 103
Somerville, R. S., Primack, J. R., & Faber, S. M. 2001, MNRAS, 320, 504
Steidel, C. C., Adelberger, K. L., Giavalisco, M., Dickinson, M., & Pettini, M. 1999, ApJ, 519, 1
Tresse, L., & Maddox, S. J. 1998, ApJ, 495, 691
Treyer, M. A., Ellis, R. S., Milliard, B., Donas, J., & Bridges, T. J. 1998, MNRAS, 300, 303
Xu, C., Hacking, P. B., Fan, F., Shupe, D. L., Lonsdale, C. J., Lu, N. Y., Helou, G., Stacey, G. J., & Ashby, M. L. N. 1998, ApJ, 508, 576
Xu, C. K., Lonsdale, C. J., Shupe, D. L., Franceschini, A., Martin, C., & Schiminovich, D. 2003, ApJ, 587, 90
Xu, C. K., Lonsdale, C. J., Shupe, D. L., O'Linger, J., & Masci, F. 2001, ApJ, 562, 179